SAND2013-1162C

Flux Characterization System for Long-Distance Heliostats

Jeremy Sment, Clifford K. Ho, Adam C. Moya, Cheryl Ghanbari
Concentrating Solar Technologies Department
Sandia National Laboratories
P.O. Box 5800, Albuquerque, NM 87185-1127, USA
(505) 845-3447, jsment@sandia.gov.

Abstract

Concentrating solar thermal power tower plants with capacities of 100 MWe or greater require large heliostat fields with heliostats over 1,500 m (nearly a mile) away from the tower. The accuracy and performance of these heliostats must be evaluated and understood as new heliostat designs emerge to reduce costs. Conventional beam characterization systems that use photographs of the reflected beam on a tower-mounted target are typically not large enough to capture the beam at large distances, and the magnitude of the irradiance for long-distance heliostats is quite low (only a fraction of a sun), which can make the beam image difficult to discern from the ambient lighting on the target. This paper describes a new system that has been developed to more accurately evaluate the flux distribution received from these long-distance heliostats to ensure that they meet requirements for optical accuracy and intensity.

A portable tool has been developed to profile the beam shape and flux intensity of heliostats at distances up to and exceeding 1700 m. The Long-Range Heliostat Target (LRHT) is a vertical array of collimated pyranometers deployed to a test site via flat-bed trailer and quickly erected on an aluminum truss tower. Once the sensors have been aimed at the heliostat, the heliostat beam is swept azimuthally across the array and the sensor data are stitched into a flux map indicating horizontal and vertical beam dimensions and flux intensities.

The LRHT was used to evaluate beam shape, peak flux, and total power of heliostats and single facet reflectors at distances from 200-1700 meters. Results were compared to theoretically rendered flux maps created by computational ray tracing algorithms, and to IR-filtered, visual band-filtered and non-filtered photographs taken on the beam characterization system (BCS) at the National Solar Thermal Test Facility at Sandia National Laboratories. Keywords: flux map, beam characterization, long-distance heliostat.

1. Introduction

Concentrating solar thermal power tower plants with capacities of 100 MWe or greater require large heliostat fields, with heliostats over 1,500 m (nearly a mile) away from the tower. The accuracy and performance of these heliostats must be evaluated and understood as new heliostat designs emerge to reduce costs. Conventional beam characterization systems that use photographs of the reflected beam on a tower-mounted target are typically not large enough to capture the beam at large distances, and the magnitude of the irradiance for long-distance heliostats is quite low (only a fraction of a sun), which can make the beam image difficult to discern from the ambient lighting on the target. This paper describes a new system that has been developed to more accurately evaluate the flux distribution received from these long-distance heliostats to ensure that they meet requirements for optical accuracy and intensity.

2. Approach

The reflected beam from the heliostat is characterized using low cost photodiode-based LI-COR LI-200SA pyranometers that were fitted into PVC collimators [1]. The collimation makes pyranometers respond like pyrheliometers by only allowing light at less than a 5˚ angle-of-incidence to reach the sensor. In this configuration the LI-COR flux reading

agrees with the Eppley normal incidence pyrheliometer (NIP) within 0.5%, but costs approximately 90% less and has a much faster response time. A long-range mobile target was constructed that is comprised of a lightweight telescoping aluminum tower mounted on a flatbed trailer. The collimated pyranometers were mounted in a vertical column over the height of the tower, aimed at the heliostat, and wired to an onboard solar powered data acquisition system. During a test, the heliostat beam is swept horizontally across the column of sensors at an even rate. The values are logged at high frequency yielding an irradiance distribution along discrete vertical transects corresponding to the heights of the sensors. The transects are then stitched together and interpolation is used to render the entire irradiance distribution.

3. Long-distance target assembly

3.1. Trailer and Truss Tower

The prototype test apparatus consists of a 15 m tall two-tier triangular truss frame aluminum tower. The tower is bolted to a thick steel base plate that has been welded onto the steel I-beams of a flat-bed trailer. The tower is supported by six pre-tensioned steel guy wires attached at one end to the designated mounting points on the tower, and at the other to three concrete blocks. Concrete blocks may be used in lieu of ground anchors when ground penetration is not possible. The trailer is stabilized by four 7 m outriggers attached to a junction that has been welded to the trailer. (Figure 1) When in position, the tower can withstand windspeeds exceeding 45 m/s (~100 mph).

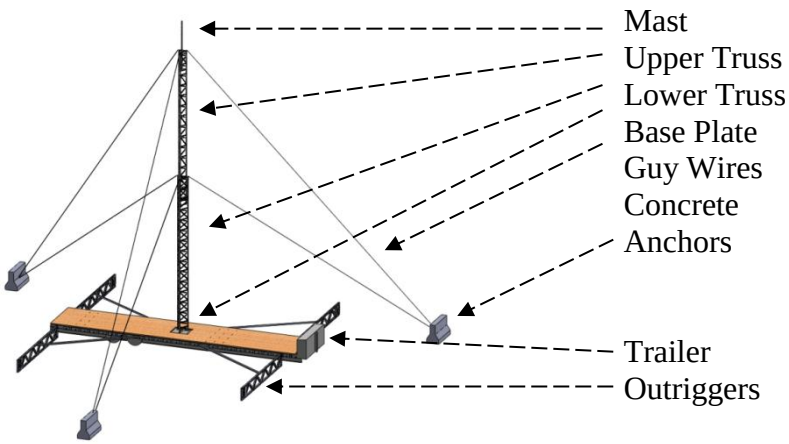

Figure 1: Long-range heliostat target assembly

3.2.1 Collimated Pyranometers

The cost of a LI-COR 200SL50 is approximately $300. A pyrheliometer can cost approximately $3000. The collimation process requires inexpensive PVC tubing and can be assembled in 20 minutes. A plastic collimator tube is painted black on the inside and fitted with baffles such that it has the same acceptance range as a thermopile pyrheliometer. The tube is placed over the pyranometer and a clear plastic lens was used to seal the column at the opposite end. (Optical information is not available on the clear plastic lens.) Twenty-seven collimated pyranometers are mounted in a vertical column over the height of the tower, aimed at the heliostat, and wired to an onboard data acquisition system housed in a weather proof enclosure (Figure 2). The data aquisition computer is powered off-grid by a 225 W solar panel and 24V battery assembly.

Figure 2: Left: Collimated LI-COR pryanometer [1]. Middle: Photo of trailer-mounted mobile heliostat target with NSTTF central receieiver tower in background. Right: close-up of collimated pyranometers mounted on aluminum tower.

3.2.2 Pyranometer response

LI-200 pyranometers have a linear response range up to 3000 W/m^2 which is adequate for long distance heliostats but often too low to characterize heliostats at close range. Furthermore these pyranometers may warp if the temperature exceeds 80° C. The resolution is approximately 0.1 W/m^2. LI-200 have a bias error of 1% up to 3000 W/m^2 and a random error up to 5% and a stability error less than 2% per 1 year period. The sensors used in this paper are less than 2 years old.

The LRHT requires a fast response time from the sensors. A complete beam sweep typically takes less than three seconds. The LI-COR LI-200 specifies a response time of 10μs while the Eppley NIP specifies a 1 second response time. Both devices were mounted and pointed at a heliostat beam while voltage was logged at 100 Hz in order to characterize the data from each type of sensor (Figure 3). Figure 4 shows that the LI-COR was able to reach its final voltage sooner than the NIP. Unlike the NIP, the LI-COR is sensitive to the periodic tracker adjustments which can be seen to occur every 10 seconds.

Figure 3: Eppley NIP (left) and Collimated LI-COR LI-200 (right) are aimed at a heliostat to test for response time.

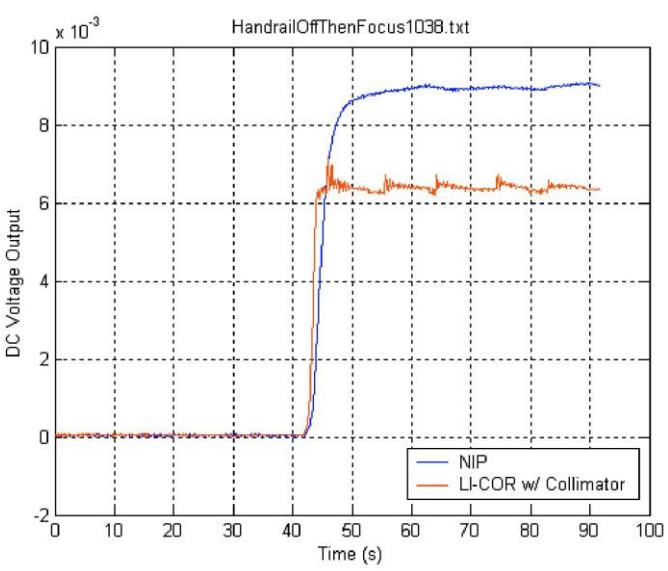

Figure 4: Uncalibrated voltage response of LI-COR and Eppley NIP. (Figure provided courtesy of Dan Fisher)

3.2.3 Pyranometer Calibration

The pyranometers were calibrated using a technique pioneered by David King et al that uses a fourth order polynomial fit to flatten the spectral response of the LI-200 so that it behaves more like a broadband pyrheliometer accross its spectral range. [4] Figure 5 shows the standard spectral reponse of the LI-200SA (in green) along with the

extraterrestrial and sea-level irradiance at AM1.5 curves. Figure 6 shows the calibrated spectral irradiance curves which exhibit a sharper rise, a flattened response, and are skewed to peak near 500 nm wavelength as does the solar irradiance at 1.5 atm. The irradiance is a function of the measured pyranometer response, temperature, and a dimensionless polynomial function of airmass. The coefficients to the polynomial were adopted from King‘s paper.[4]

During the calibration process the collimated pyranometer and an Eppley pyrheliometer were pointed directly at the sun. Data was logged continuously from one hour before airmass would have been 1.5 to one hour after. A calibration constant (C_n) was then calculated to fit the pyranometer response to the pyrheliometer under specific conditions. Logged data from the sweep was adjusted for airmass other than 1.5 using the King/Boyson equation.

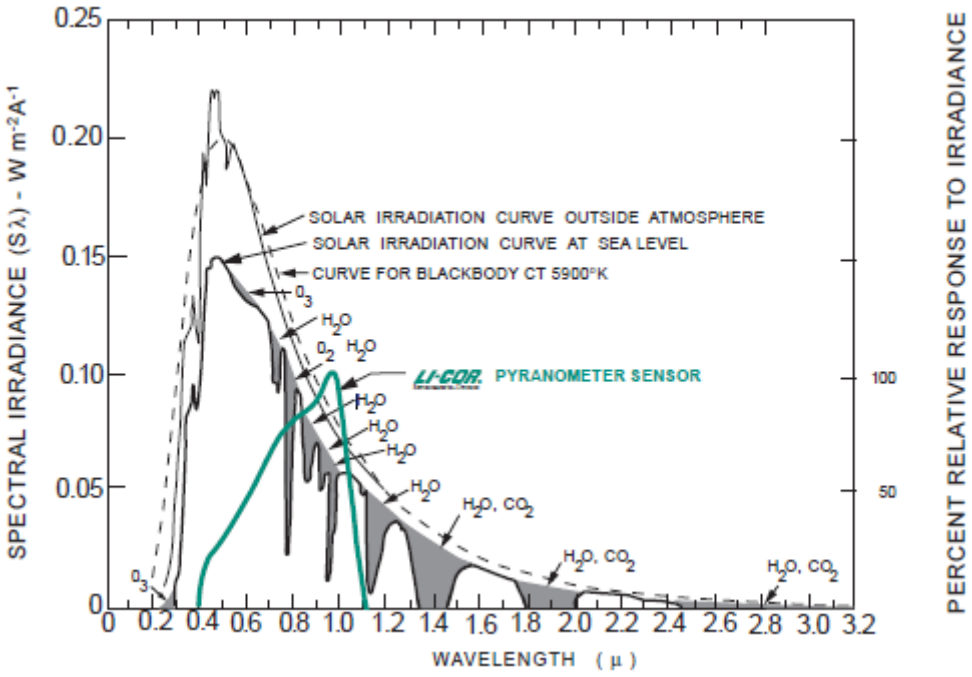

Figure 5: The LI-200SA pyranometer spectral response is overlayed with the extraterrestrial solar irradiance and the solar irradiance at Air Mass = 1.5 (Copyright Licor Inc. Used by Permission)

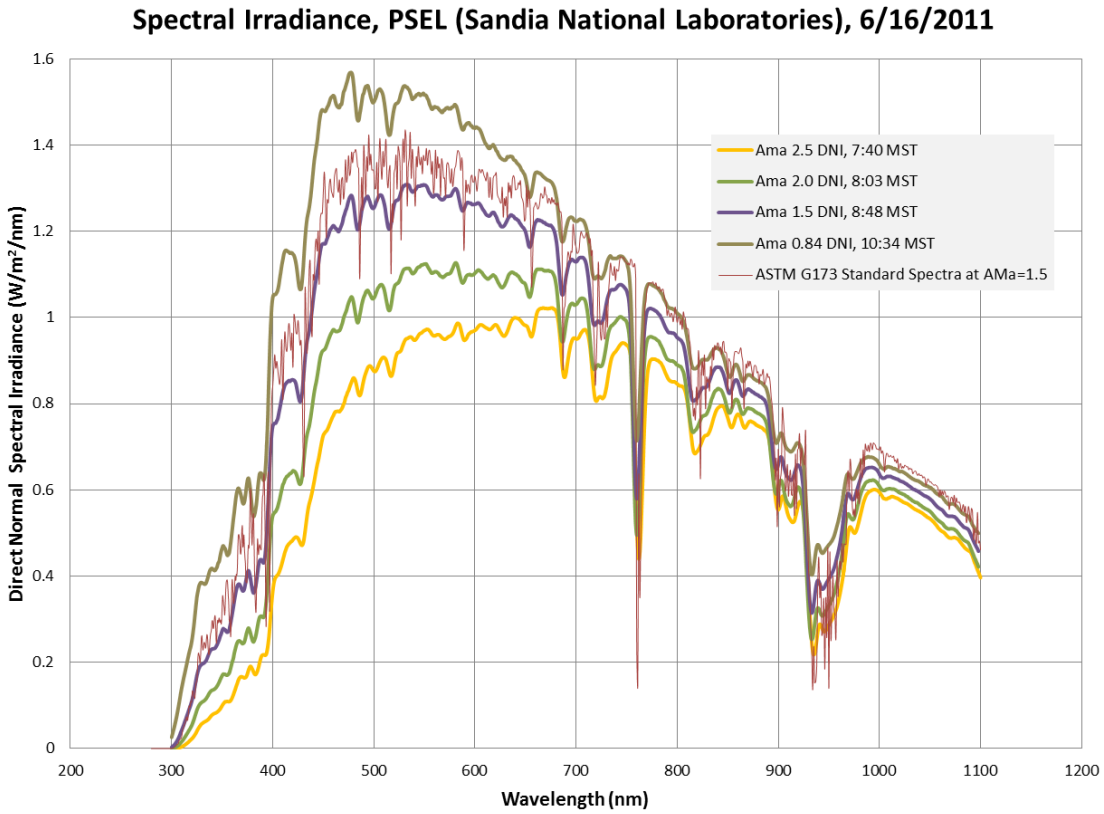

Figure 6: Spectral Irradiance curves of calibrated LI-COR LI-200 pyranometers based on data measured at different air mass, and the ASTM G173 standard spectra at Ama=1.5. Data taken at Photovoltaic Systems Evaluation Laboratory (PSEL) at Sandia National Laboratories by Jay A. Kratochvil. Used by permission.

4. Operational Procedure

4.1. Aiming Sensors

The collimated pyranometers are mounted in an aiming assembly made of hardware that allows horizontal and vertical adjustment. The horizontal range in which the sensor can be pointed is approximately 90° and the vertical range is 180°. While the heliostat beam is set to track on the center of the target, each sensor must be hand aimed by a technician.

An aiming tool which accompanies the technician on a boom lift creates a beeping sound while the sensor is reading a value within 2% of the maximum irradiance that particular sensor has registered during the aiming process. The beeping sound is convenient as glare

may inhibit monitor visibility. The technician then sweeps the sensor across the incident beam horizontally until the beeping stops. The sensor is then slowly returned to center until the beeping returns at which point the sensor is in its optimal horizontal location. The process is then repeated with vertical rotations. Each sensor takes less than five minutes to point so light variation due to solar position is not ordinarily a significant factor.

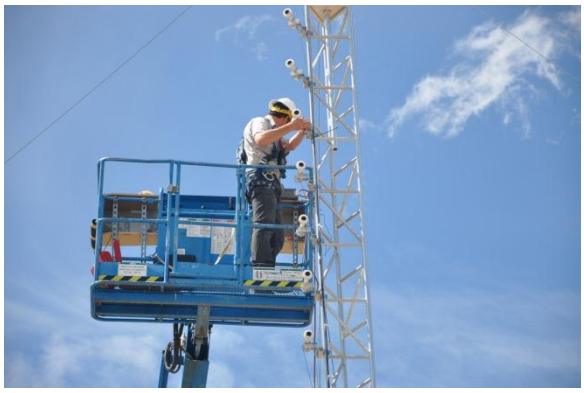

Figure 7: Technician aims sensor at a light source.

4.2. Acquiring Data and Interpolating image

Calibrated data from the LRHT is rendered as a contour plot. The horizontal x-axis represents the beam width and is the product of sweeprate, distance, and time. Sweeprate is a function of the mechanical sweeprate, and the sun‘s position. The mehanical sweep rate (rad/sec) is muliplied by 2 to account for the half-angle effect which causes the beam to move at twice the speed of the reflector. The horizontal component must then be extracted by dividing the nominal beam sweep rate by cosine of the solar elevation half-angle. The sweep time of each sample is calculated as the sample index divided by the sampling rate of the data acquisition system. The physical heights of the anemometers in meters constitute the vertical y-axis. Linear interpolation is used to provide an equal number of datapoints in the x and y directions to create a mesh upon which irradiance data can be plotted.

5.1 Evaluation

A test heliostat and individual facets were used to validate the LRHT's performance. The test heliostat beam was ~340 m from the target and had a sweeprate of 2.6 mrad/s with a neglible standard deviation. Individual facets were positioned 512 m and 1733 m from the target and mounted on a single-facet rig. The single-facet rig employed a hand powered turnbuckle as an azimuth drive and therefore had variability in the sweep rate. In order to estimate the rig's sweep rate, five timed trials were performed where the technician swept the facet a known angle. The average sweep rate of 4.7 mrad/s was used. The standard deviation was about .26 mrad/sec.

The peak flux values measured by the pyranometers have up to 8% error from the LICOR pyranometers plus 2% error from the aiming process plus .78% calibration error. The background irradiance entering the collimated sensor was on the order of 2 W/m^2 and was subtracted from the flux measurements. A generalized error of 10% was applied to stated flux values. The pyranometer heights were measured from the deck of the trailer and are accurate to 1.25 cm. The plotted height on the y-axis may be cropped if the beam exceeded the height of the tower. The mechanical sweep rate of the portable hand-cranked facet rig was determined by measuring the average time required to rotate the test heliostat a known angle. Solar position was provided by the Solar Position Algorithm. The distance to the heliostat was measured with an optical range finder. The distances to the 512 m and 1733 m tests were estimated using Google maps.

6. Results

6.1. Test Heliostat at 337 meters January 5, 2012

On January 5, 2012 at solar noon, the test heliostat was swept across the LRHT. Figure 8 shows a theoretical irradiance distribution on the LRHT from the test heliostat calculated using ray tracing. While the precise reflectivity and slope error of the test heliostat is not known, a reflectivity of .85 and RMS slope error of 1 mrad was chosen as a best estimate.

Figure 9 shows the measured irradiance distribution as rendered by the LRHT at the same time and date.

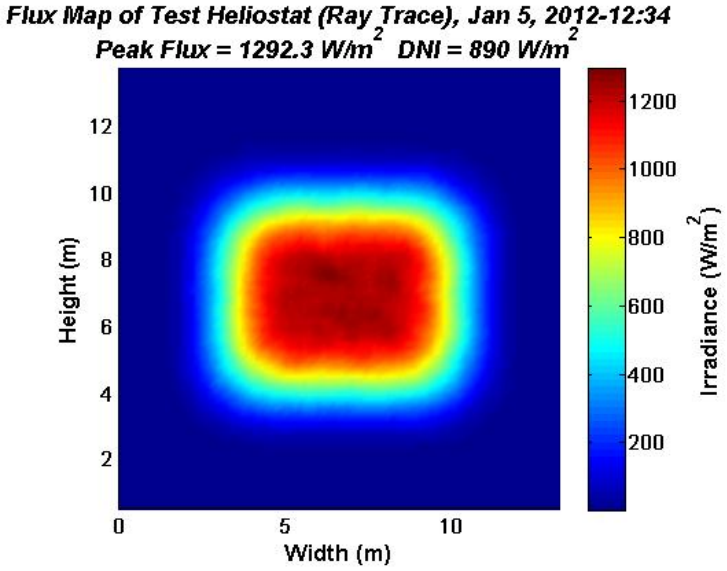

Figure 8: Simulated irradiance distribution on the long-range heliostat target on January 5, 2012 at 12:34 pm. reflectivity=.85, slope error = 1 mrad, DNI=890, Focal length=1500m, peak flux = 1292 W/m2

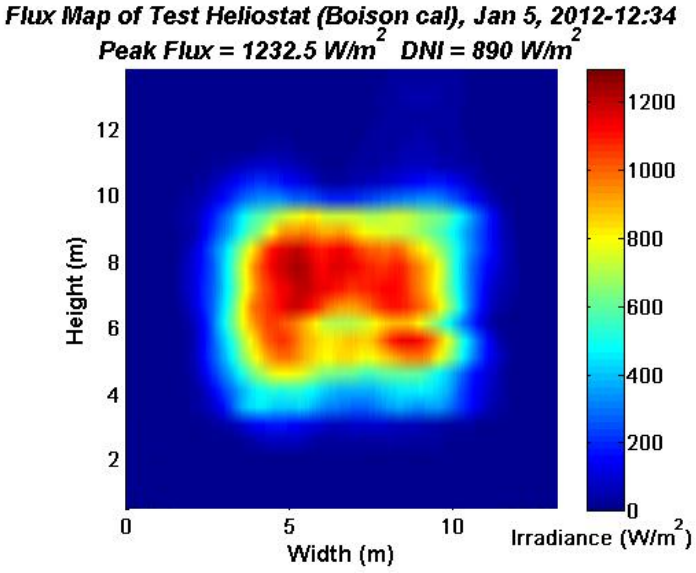

Figure 9: Flux map of test heliostat beam as rendered by LRHT on January 5, 2012 at 12:34 pm. DNI=890, peak flux = 1233 W/m2

The overall size and shape of the theoretical and empirical images have many similarities. The peak flux, total power, and beam dimensions containing 95% of the total power of the beam image were compared for validation. Table 1 summarizes the differences between

the two methods of beam characterization. The peak flux measurements show agreement between the two methods within the 11% margin of uncertainty (see 2.2.1). The theoretical peak flux under the specified conditions was 1292 W/m^2 while the measured peak flux was 1233 W/m^2. Power was estimated by multiplying the measured flux value by the area contained in the sample which is the difference in sensor heights multiplied by the x-distance per sample. Total power of the LRHT image is presumed to be the sum of all power calculations over all cells.

The beam dimensions containing 95% of the power were based on the distance from the centroid. The centroid's x coordinate was determined by multiplying each power value by the distance from the origin, summing all these moments, and dividing by the total power value. The percentage of power contained in each row across all columns was calculated and added to the adjacent row moving from the centroid outward to the edges such that approximately 50% of the power is to the left of the centroid and 50% is to the right. The beam width is then specified as the difference between the width measurements corresponding to 47.5% of the power on either side of the centroid. The process was repeated in the y dimension to specify the beam height. The results show significant error in the width and height measurements. Factors influencing the discpreancies in beam shapes include differences in facet canting and focusing.

	Ray Trace Prediction	LRHT	Median Error
Peak Flux	1,292 W/m^2	1,233 W/m^2	.05
Total Power	46326 W	41204 W	.11
95% Beam Width	7 m	7.9 m	.14
95% Beam Height	5.9 m	4.8 m	.19

Table 1: Peak Flux, and beam shape data as rendered by the Ray Trace method, and the Long Range Heliostat Target.

6.2 Test Heliostat July 19

Tests were taken throughout the day on July 19 to assess the LRHT's qualitative ability to render the changing beam shape over the day. The beam characterization system (BCS) procedure takes digital photographs of the central receiver tower wall with and without a beam. The pixel saturation values of the tower wall without the beam are subtracted from the saturation values with a beam. Camera specific constants are then used to convert pixel saturation to flux values. The images in Table 2 show good agreement with the BCS images taken on the central receiver tower located due west of the LRHT and the ray trace model of the beam at the LRHT location. While it is expected that the beam shape will differ in separate locations there are some details that can be identified in both. At 8:00 am the LRHT and the BCS images both represent two hot spots within the beam shape. The slope is in the same direction throughout the day. As expected, the LRHT image is narrower due to it being more normal to the test heliostat. At solar noon, the remote target correctly rendered some detailed anomalies such as the horseshoe shape.

	LRHT	BCS Image on Central Receiver Tower	Ray Trace
8am	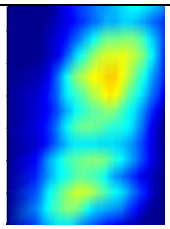	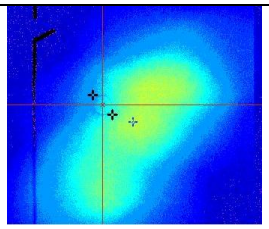	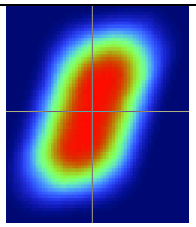
11am	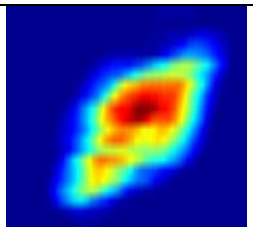	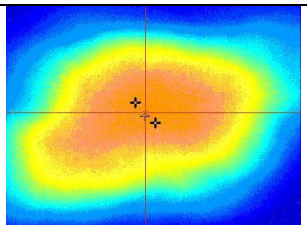	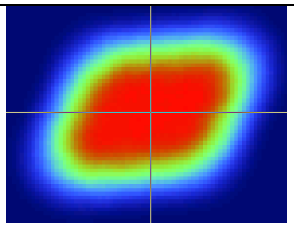
1pm (Solar Noon)	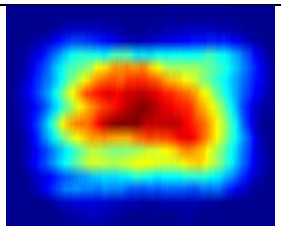	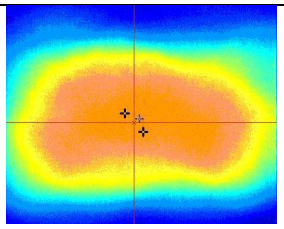	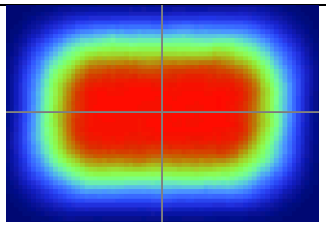
2pm	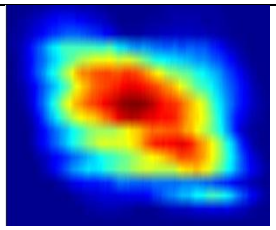	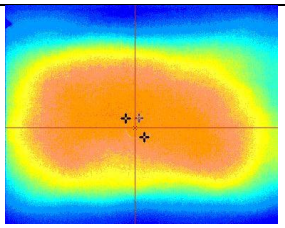	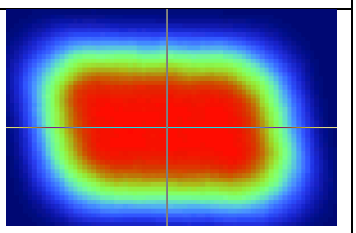

Table 2: Qualitative comparison of beam shape as rendered by three methods at different times of day.

The image taken at solar noon has been singled out for more quantitative validation in Figure 10 and Figure 11. The peak flux value of ~1325W/m^2 is near the predicted value. The estimated total power is close to the theoretical value based on the specified reflectivity. There is more significant error in the height dimension. There is an indication in the image that 95% of the power may be distributed across a narrower height band than is predicted by ray tracing. The results from the three methods are summarized in Table 3.

	Ray Trace Prediction	LRHT	Relative Error
Peak Flux	1296 W/m^2	1325 W/m^2	.02
Total Power	38160 W	33759 W	.08
95% Beam Width	8.0 m	7.5 m	.06
95% Beam Height	5.9 m	4.3 m	.27

Table 3: Peak Flux, total power, and beam dimensions containing 95% of total power as rendered by the Ray Trace method, and the Long Range Heliostat Target.

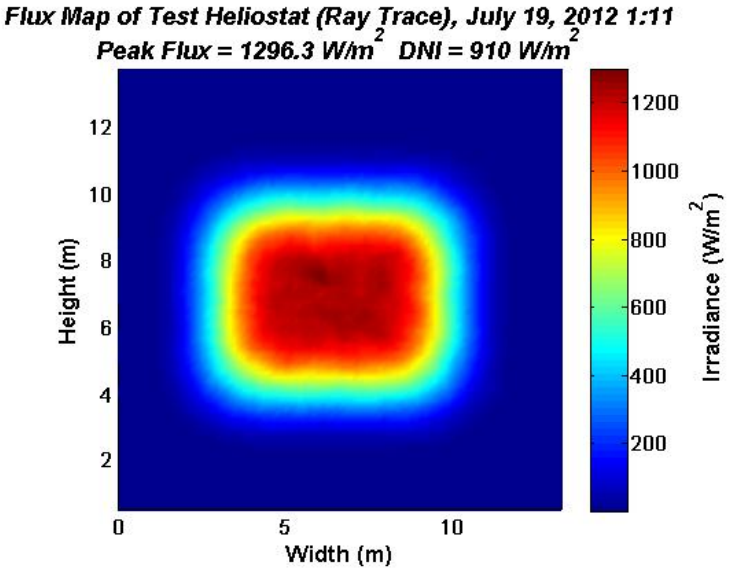

Figure 10. Simulated irradiance distribution on the long-range heliostat target at 1:11pm, July 19, 2012, DNI = 910 W/m^2, RMS slope error = 1 mrad, reflectivity = 0.85, focal length = 1500 m. Peak flux=1,296W/m^2.

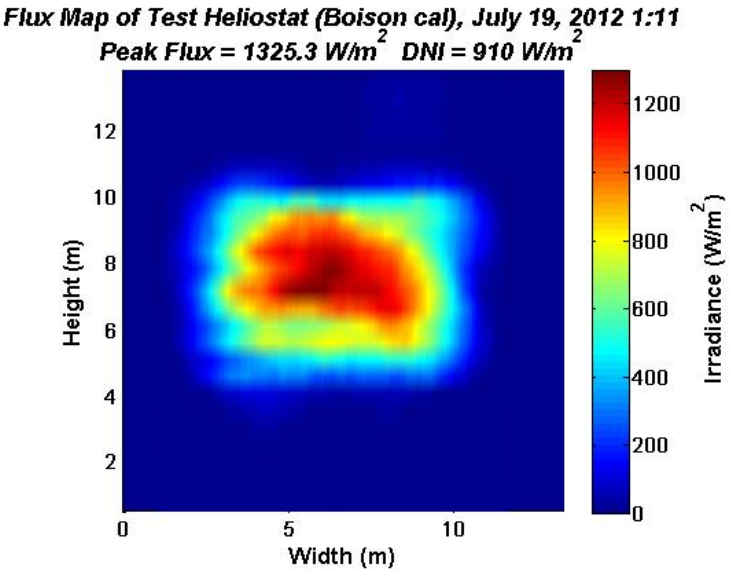

Figure 11: Flux map of test heliostat beam as rendered by LRHT on July 19, 2012 at 1:11pm. DNI=910, peak flux = 1325 W/m2

6.3 Single Facets at 512 and 1700 meters

The LRHT was used to characterize single facets at distances of 512 m and 1733 m. The faint images at this distance could not be detected with the BCS system. Figure 12 shows the relative performace of a silver backed glass 1.49 m^2 facet and a reflective film facet of the same size at distances of 512m. The edges appear coarse due to the hand-turned mechanism used to sweep the image. Hence the width of the beam may contain additional uncertainty. The relative intensities can provide information on how such films may perform if installed by a utility.

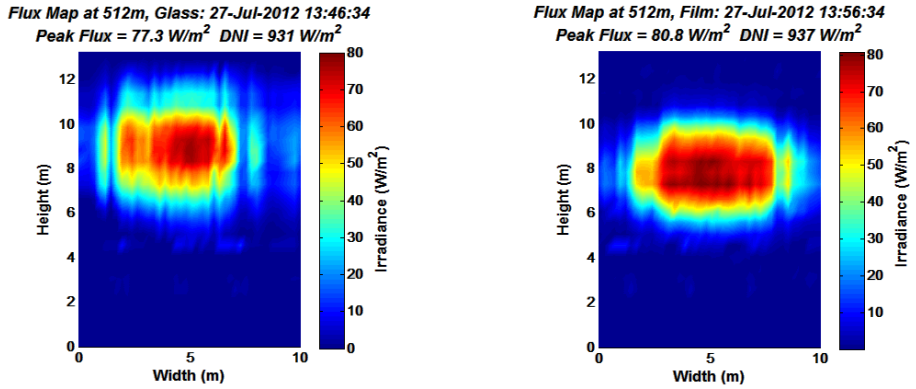

Figure 12: LRHT flux maps of two single facets made glass (left) and reflective film (right).

Figure 13 shows one of the same facets relocated to a point 1733m (1.1 miles) away. (The beam in the figure is not pointed directly at camera.) While the light from this beam was not detectable on the central receiver tower, the LRHT was able to provide information on the relative performance of two different facets at distances often attained by the extremities of large scale heliostat fields. (Figure 14). Again, the width indicated in the plot may be inaccurate due to the hand activated azimuth mechanism on the single-facet rig resulting in an uneven sweep rate. The peak flux measurements of the facets at 1733 are near 1/100th of a sun. Beam image details are not well rendered at this distance but information on the flux and basic size of the beam particularly the y axis, may help predict performance of a long-distance heliostat before it is installed..

Figure 13: Left: Facet as seek from the portable target at a distance of 1733 m. Right: Map image of facet locations with lines drawn to target. © Google 2012.

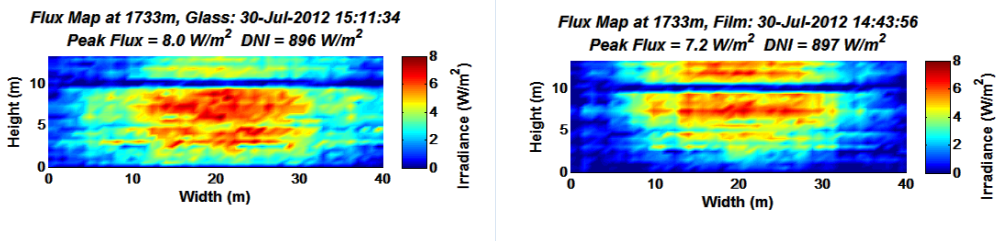

Figure 14: LRHT flux maps of two single facets made of glass (left) and reflective film (right) at a distance of 1733 m.

7. Summary

The long-range heliostat target (LRHT) has shown a promising ability to quickly and accurately characterize heliostats and facets at long distances. The target is portable and can be driven via flatbed trailer to a test site and quickly assembled. The low-cost LI-200 pyranometers are collimated and calibrated to behave similarly to more expensive Eppley pyrheliometers. A heliostat was tested at a distance of ~340 m and two single facets were tested at ~500 and ~1700 m. Flux values were logged as the beams were swept horizontally across the column of sensors at an even rate yielding an irradiance distribution along discrete vertical transects corresponding to the heights of the sensors. Interpolation was then used to render the entire irradiance distribution into a flux map. The peak flux and estimated height and width of the interpolated beam image were compared to the results of a beam analysis modeled by ray tracing. Qualitative features in the beam images rendered by the LRHT were compared to images taken on the nearby central receiver tower and show many similarities. In the case of the single facets at 1700 m, while the beam image was not detectable on the face of the central receiver tower, the long-range heliostat target was able to measure the flux and provide a fuzzy but informative beam image.

Acknowledgements

The authors thank Mark Speir, Roger Buck, J.J. Kelton, Daniel Ray, Kye Chisman, Dan Fisher, and Greg Kolb for their assistance with the testing and development of the system. Sandia National Laboratories is a multi-program laboratory managed and operated by Sandia Corporation, a wholly owned subsidiary of Lockheed Martin Corporation, for the U.S. Department of Energy's National Nuclear Security Administration under contract DE-AC04-94AL85000.

References

[1] Duffie, J. A., & Beckman, W. A. (1991). *Solar Engineering of Thermal Processes* (2nd ed.). New York, New York: John Wiley & Sons, Inc.

[2] Ineichen, P., & Perez, R. (2002). A New Airmass Independent Formulation of the Linke Turbidity Coefficient. *Solar Energy*, *73*, 151-157.

[3] King, D. L., & Meyers, D. R. (1997). Silicon-Photodiode Pyranometers: Operational Characteristics, Historical Experiences, and New Calibration Procedures. *IEEE 26th PVSC Sept. 30-OCt. 3, 1997* (pp. 1285-1288). Anaheim, CA: IEEE.

[4] King, D. L., Boyson, W. E., & Bower, W. I. (1998). Improved Accuracy for Low-Cost Solar Irradiance Sensors. *2nd World Conference and Exhibition on Photovoltaic Solar Energy Conversion, 6-10 July 1998.* Vienna, Austria: Sandia National Laboratories.

[5] King, D. L., Kratochvil, J. A., & Boyson, W. E. (1997). Measuring Solar Spectral and Angle-of-Incidence Effects on Photovoltaic Modules and Soalr Irradiance Sensors. *26th PVSC; Sept. 30-Oct. 3, 1997* (pp. 1113-1116). Anaheim, CA: IEEE.

[6] Maxwell, E. L. (1987). *A Quasi-Physical Model for Converting Hourly Global Horizontal to Direct Normal Insolation* (Vols. SERI/TR-215-3087). Golden, CO: Solar Energy Research Institute.

[7] Perez, R. R., Ineichen, P., Maxwell, E. L., Seals, R. D., & Zelenka, A. (1992). Dynamic Global-to-Direct Irradiance Conversion Models. *ASHRAE*, 354-369.

[8] Perez, R., & Ineichen, P. (1987). A new simplified version of the Perez Diffuse Irradiance model for tilted surfaces. *Solar Energy*, 221-231.

[9] Perez, R., & Ineichen, P. (1990). Modeling daylight availability and irradiance components from direct and global irradiance. *44*.

[10] Perez, R., & Ineichen, P. (2002). A New Operational Model for Satellite-Derived Irradiances: Description and Validation. *Solar Energy, 73*(3), 307-317.

[11] Reda, I., & Andreas, A. (January 2008). *Solar Position Algorithm for Solar Radiation Applications.* Golden, Colorado: NREL.